A Novel Model Predictive Current Control With Reduced Computational Burden Based on Discrete Space Vector Modulation for PMSM Drives

Jun SUN, Yong YANG, Jiefeng HU, Xinan ZHANG, Xinghe LI, and Jose RODRIGUEZ

***Abstract*—Discrete space vector modulation (DSVM) technique is commonly adopted in model predictive control (MPC) to mitigate current harmonics and torque ripples. Nevertheless, the employment of DSVM typically leads to heavy computational burden and high switching frequency (SF). To solve these problems, a novel model predictive current control (MPCC) scheme based on DSVM is proposed in this paper for permanent magnet synchronous motor (PMSM) drives. Firstly, a simple voltage vectors (VVs) pre-selection strategy based on the stator flux increment is introduced to eliminate the redundant virtual VVs generated by DSVM for the purpose of lower computational burden. Then, a hierarchical search strategy is designed to generate the candidate VVs online, which can further simplify the DSVM technique. In addition, an efficient optimal switching sequence (OSS) method is also employed to reduce the switching losses without weakening the control performance. Compared to the existing strategies, the proposed scheme possesses lower complexity and SF as well as superior performance. The effectiveness of the proposed scheme is supported by comparative experimental results on a PMSM platform.**

***Index Terms*—Discrete space vector modulation (DSVM), low complexity, model predictive current control (MPCC), permanent magnet synchronous motor (PMSM), pre-selection strategy, reduced switching frequency.**

Manuscript received March 1, 2024; revised May 3, 2024; accepted May 25, 2024. Date of publication September 30, 2024; date of current version June 11, 2024. This work was supported in part by the National Natural Science Foundation of China under Grant 52377195, in part by the Transformation of Scientific and Technological Achievements in Suzhou (Carbon Peak Carbon Neutral Project) under Grant ST202303, in part by through projects FB0008, 1210208 and 1221293. *(Corresponding author: Yong Yang.)*

J. Sun and Y. Yang are with the School of Rail Transportation, Soochow University, Suzhou 215131, China (e-mail: jsun98@stu.suda.edu.cn; yangy1981@suda.edu.cn).

J. Hu is with the Centre for New Energy Transition Research, and with the Institute of Innovation, Science and Sustainability, Federation University Australia, Mount Helen, 3353 VIC, Australia (e-mail: j.hu@federation.edu.au).

X. Zhang is with the Department of Electrical, Electronic and Computer Engineering, University of Western Australia, Perth, WA 6009, Australia (e-mail: xinan.zhang@uwa.edu.au).

X. Li is with the Product Management Department, Shanghai Sigriner STEP Electric Co., Ltd, Shanghai 201800, China (e-mail: LeeSTEP@126.com).

J. Rodriguez is with Faculty of Engineering, Universidad San Sebastian Santiago, Santiago 8370146, Chile (e-mail: jose.rodriguezp@uss.cl).

Digital Object Identifier 10.24295/CPSSTPEA.2024.00009

I. Introduction

OWING to the outstanding features, such as high efficiency, compact structure and large torque density, permanent magnet synchronous motors (PMSMs) have been widely applied in electric/hybrid vehicles, aerospace, servo drives, and robotics [1], [2]. Field-oriented control (FOC) and direct torque control (DTC) are two popular control strategies for PMSM drives. On the one hand, FOC utilizes simple PI controllers to regulate the field currents. However, the process of tuning the PI controller gains to attain an optimal trade-off between steady-state and dynamic performance is typically laborious [3]. On the other hand, DTC exhibits faster dynamic responses compared to FOC [4], whereas the classical DTC suffers from large torque and flux ripples in the steady state.

Recently, the finite control set model predictive control (FCS-MPC) has been widely implemented in PMSM drives due to the advantages of simplicity, fast dynamic response, and ease of handling nonlinear constraints [5], [6]. Compared with DTC, FCS-MPC contributes to minimizing the current or flux ripples by applying an optimal voltage vector (VV) that minimizes a user-defined cost function while respecting constraints on inputs and/or states [7], [8]. However, due to the application of only one VV in an entire switching cycle, the performance of the conventional FCS-MPC is unsatisfactory. In addition, it also leads to variable switching frequency (SF) [9]–[12].

A substantial amount of research work has been carried out to further improve the performance of FCS-MPC [12]–[19]. In [13]–[16], the multi-vector schemes with the duty cycle control principle are employed to enhance the steady-state performance. Through tracking the stator current error vector produced by the zero VV, [14] combines the optimal active VV with the zero VV and calculates their duty cycles, which help to reduce the torque ripples. In [15], [17], more generalized dual-vector approaches are proposed, which include the active VVs as the second optimal VV, and achieve the ability to regulate the phase of the output VV [15]. Additionally, to completely eliminate steady state errors, schemes combining three VVs are employed in [16]–[19], where torque ripples and current harmonics can be further reduced by synthesizing two active VVs and the zero VV. However, despite the effectiveness of the above-mentioned multi-vector MPC methods in enhancing the performance of FCS-MPC, the evaluation of the optimal

VVs and the calculation of the duty cycles remain complicated. Additionally, the utilization of multiple VVs also leads to the increased SF, making them less attractive for industrial applications [17].

In addition to multi-vector FCS-MPC, the discrete space vector modulation (DSVM) based FCS-MPC is also an effective solution [20]–[22]. With pre-dividing the control period, a large number of virtual VVs can be synthesized in the DSVM technique to improve the accuracy of the optimal VV [20]. Theoretically, the control performance can be enhanced as the subdivision degree N of the control cycle increases [21]. However, the computational burden of evaluating all VVs also increases dramatically, which hinders the further usage of DSVM [22]. Therefore, considering the balance between computational burden and performance, some studies optimized the DSVM-MPC under N=3 [22]–[25]. In [22], the number of candidate VVs is reduced from 38 to 15 by evaluating the center virtual VVs in the sector, and an online SF reduction method is proposed to decrease the SF losses. While in [23], the 38 VVs are divided into 6 control sets, and the optimal VV can be evaluated from 13 candidate VVs without suboptimality. [24] utilized the principle of DTC and selected 12 candidate VVs for evaluation based on the switching table. However, the output VV evaluated by [24] could not guarantee optimality due to the hysteresis of torque and stator flux error [23]. Moreover, it is worth noting that the computational advantage of the above schemes cannot be maintained when N grows [25].

In order to further decrease the computational effort of DSVM based MPC, several VV pre-selection strategies have been introduced in [25]–[28]. In [25], a two-step optimization method is used to determine the optimal VV based on the reference VV obtained from the deadbeat control. These optimizations aim to enhance the system performance, but the overall computational burden is still large. In [26] and [27], the number of candidate VVs to be evaluated is reduced to three by using the deadbeat torque and flux control (DB-DTFC), and the generation of VVs does not depend on the look-up table. However, the identification of candidate VVs requires complex geometric operations, which increases the complexity of the algorithm. Compared with [26], [28] improves the robustness of the system by evaluating more virtual VVs. However, the algorithm is computationally intensive when the reference VV is close to the over-modulation region. Furthermore, [29] and [30] achieve the optimal VV by solving the partial differential equations, which further improves the control performance at the cost of increased complexity. In [31], a simpler pre-selection method that only requires the flux trajectory and speed direction is employed. Meanwhile, the carrier-based PWM technique is also incorporated to obtain a fixed SF. Unfortunately, the computational burden of [31] is still high when the number of virtual VVs rises.

To overcome the aforementioned shortcomings in DSVM-based MPC, an improved model predictive current control scheme based on DSVM is proposed in this paper. The main contributions of the paper can be concluded below:

(a) Compared with existing enumeration-based strategies, such as [22], [23], [24], etc., the proposed scheme avoids the tedious evaluations for optimal VV through using a simple pre-selection method based on the stator flux increment, thereby simplifying computations.

(b) The proposed scheme ensures the optimality of output VV even as the number of virtual VVs increases, leading to performance improvement.

(c) An optimal switching sequence (OSS) strategy aimed at minimizing the number of switching is adopted to decrease the switching losses, which further enhances the application of the DSVM technique.

(d) Experimental comparisons with the all-vector-based DSVM-MPC and the existing DSVM-MPC schemes [23], [24], [26] have been conducted to emphasize the advantages of the proposed scheme.

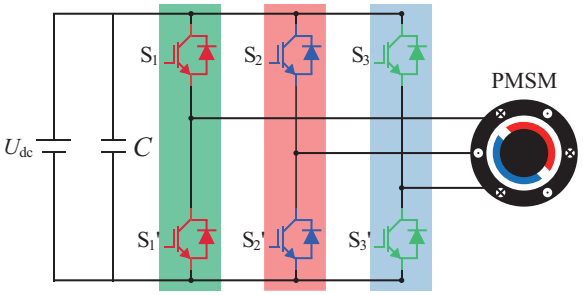

Fig. 1. Two-level three-phase PMSM inverter.

The remaining sections of the paper are arranged as follows: Section II establishes the mathematical model of PMSM drives and introduces the conventional FCS-MPCC. Section III describes the application of DSVM in FCS-MPC. In Section IV, the enhanced DSVM-MPCC scheme is proposed. Section V presents and discusses the experimental results. Finally, conclusions are drawn in Section VI.

II. Model of System and Conventional FCS-MPCC

A. System Modeling

A surface-mounted PMSM (SPMSM) is studied in this paper. As shown in Fig. 1, a two-level three-phase voltage source inverter (2L-VSI) is used to drive the PMSM. The eight basic VVs generated by the inverter can be expressed as

$$\mathrm{V}_i = \frac{2}{3} U_{\mathrm{dc}} (S_1 + aS_2 + a^2 S_3) \tag{1}$$

where U_{dc} represent the DC bus voltage; $\mathrm{V}_{i,i=0...7}$ represent the eight basic VVs; $S_{i,i=1,2,3}$ denote the switching states of the three phases and $a = \mathrm{e}^{\mathrm{j}2\pi/3}$.

Considering the symmetry of three-phase windings and the equal inductance of d- and q-axis, the mathematical model of SPMSM in the rotor reference frame can be described as

$$\boldsymbol{u}_{dq} = R_{\mathrm{s}} \boldsymbol{i}_{dq} + \frac{\mathrm{d}\boldsymbol{\psi}_{dq}}{\mathrm{d}t} + \omega_{\mathrm{e}} \begin{bmatrix} 0 & -1 \\ 1 & 0 \end{bmatrix} \boldsymbol{\psi}_{dq} \tag{2}$$

$$\boldsymbol{\psi}_{dq} = L_s \boldsymbol{i}_{dq} + \boldsymbol{\psi}_{rf} \tag{3}$$

$$T_e = \frac{3}{2} p i_q \left[i_d \left(L_d - L_q \right) + \psi_f \right] \tag{4}$$

where $\boldsymbol{u}_{dq} = [u_d \ u_q]^T$, $\boldsymbol{i}_{dq} = [i_d \ i_q]^T$, $\boldsymbol{\psi}_{dq} = [\psi_d \ \psi_q]^T$are the stator voltage vector, stator current, stator flux in *d*-*q* axes respectively; R_s is the stator resistance; $L_s = L_d = L_q$ is the synchronous inductance; $\boldsymbol{\psi}_{rf} = [\psi_f \ 0]^T$, where ψ_f is the rotor flux; T_e is the electromagnetic and p is the number of pole pairs.

Supposing that the motor velocity is constant within a single control cycle, the discrete model for the current prediction of the SPMSM in the rotor reference frame can be obtained by the first-order Euler approximation as

$$\boldsymbol{y}(k+1) = \boldsymbol{A}\boldsymbol{y}(k) + \boldsymbol{B}\boldsymbol{x}(k) + \boldsymbol{C} \tag{5}$$

where $\boldsymbol{y} = [i_d \ i_q]^T$, $\boldsymbol{x} = [u_d \ u_q]^T$, and

$$\boldsymbol{A} = \begin{bmatrix} 1 - \dfrac{R_s T_s}{L_s} & \omega_e T_s \\ -\omega_e T_s & 1 - \dfrac{R_s T_s}{L_s} \end{bmatrix}, \boldsymbol{B} = \begin{bmatrix} \dfrac{T_s}{L_s} & 0 \\ 0 & \dfrac{T_s}{L_s} \end{bmatrix}, \quad \boldsymbol{C} = \begin{bmatrix} 0 \\ -\dfrac{\omega_e \psi_f T_s}{L_s} \end{bmatrix}.$$

where $i_d(k), i_q(k)$ are the *d*- and *q*-axis stator currents at instant k; $u_d(k), u_q(k)$ are the *d*- and *q*-axis stator voltages at instant k; $i_d(k+1)$, $i_q(k+1)$ are the *d*- and *q*-axis stator currents at instant $k+1$; T_s is the sampling period; ω_e is the rotor velocity.

B. Conventional FCS-MPCC

In the SPMSM drive system, the electromagnetic torque is proportional to the *q*-axis stator current. To achieve a good system response and maximize electromagnetic torque, the generated current vector usually needs to be concentrated in the *q*-axis direction under the operating conditions below the rated speed. Hence, in the conventional FCS-MPCC scheme, the reference *q*-axis stator current is provided by a speed loop comprising a PI controller, and the reference *d*-axis stator current is usually set to 0.

Based on (5), conventional FCS-MPCC firstly predicts the current vector generated by each basic VV. Then, the predicted current is substituted into the cost function for iterative evaluation of VVs.

In addition, one-step compensation is employed to compensate for the time delay [11]. Consequently, the cost function can be defined as

$$\begin{cases} g(i) = \left\| i_d^* - i_d(k+2) \right\|_2 + \left\| i_q^* - i_q(k+2) \right\|_2 \\ \mathrm{VV}_{opt} = \arg\min[g(i)]_{i=0\ldots7} \end{cases} \tag{6}$$

Therefore, the conventional FCS-MPCC can achieve better dynamic performance compared to FOC and DTC by optimizing the output of the optimal VV online in each cycle.

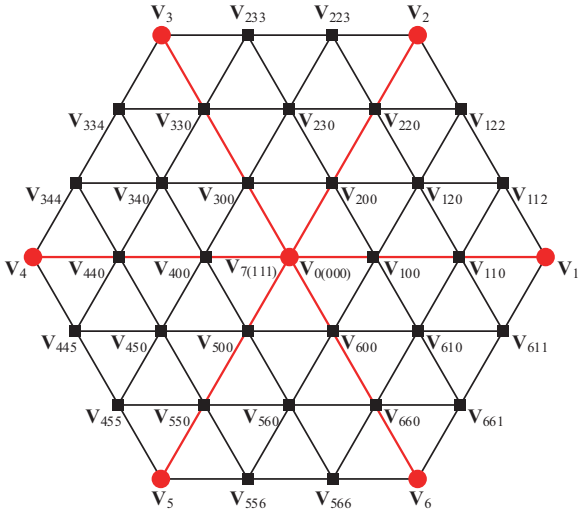

Fig. 2. Spatial distribution of VVs when using DSVM (*N*=3).

III. FCS-MPCC Based on DSVM

For conventional FCS-MPCC schemes, the available VVs only include six active VVs and two zero VVs. This limitation leads to large torque ripples and current harmonics in the steady-state [8]. To address this problem, the discrete space vector modulation (DSVM) technique is introduced to expand the available control set of FCS-MPCC. In the DSVM, every control cycle is divided into N parts evenly according to the pre-definition, and a heavy quantity of virtual VVs will be synthesized in each interval by utilizing basic VVs, which can be described as

$$\mathrm{V}_{vir} = \sum_{i=1\ldots N} t_i \mathrm{V}_i^{basic} \tag{7}$$

$$t_i = \frac{T_s}{N} \tag{8}$$

$$\mathrm{V}_i^{basic} \in \{\mathrm{V}_0, \mathrm{V}_1, \ldots, \mathrm{V}_7\} \tag{9}$$

At the same time, the final number of available VVs can be calculated by the number N as

$$n_{vvs} = 3N^2 + 3N + 2 \tag{10}$$

Considering the complexity of the VVs table, the number N is usually taken as 3, and the corresponding VVs distribution is shown in Fig. 2. All VVs can be classified into three types:

- Type-I: it only contains one basic VV in a single control cycle, such as $\mathbf{V}_{0(000)}$, $\mathbf{V}_{1(111)}$.
- Type-II: it consists of one active VV and one zero VV in a single control cycle, such as $\mathbf{V}_{110}$, $\mathbf{V}_{220}$.
- Type-III: it consists of two active VVs and one zero VV in a single control cycle, such as $\mathbf{V}_{120}$, $\mathbf{V}_{230}$.

The Table I shows the composition of virtual VVs for *N*=3, and there are similar synthesis schemes for other N values. It

TABLE I
SYNTHESIS OF VIRTUAL VVS (N=3)

Virtual VVs	Synthesized by basic VVs	Virtual VVs	Synthesized by basic VVs
$\mathbf{V}_{100}$	$(\mathbf{V}_1 + 2\mathbf{V}_0) / 3$	$\mathbf{V}_{110}$	$(2\mathbf{V}_1 + \mathbf{V}_0) / 3$
$\mathbf{V}_{200}$	$(\mathbf{V}_2 + 2\mathbf{V}_0) / 3$	$\mathbf{V}_{220}$	$(2\mathbf{V}_2 + \mathbf{V}_0) / 3$
$\mathbf{V}_{300}$	$(\mathbf{V}_3 + 2\mathbf{V}_0) / 3$	$\mathbf{V}_{330}$	$(2\mathbf{V}_3 + \mathbf{V}_0) / 3$
$\mathbf{V}_{400}$	$(\mathbf{V}_4 + 2\mathbf{V}_0) / 3$	$\mathbf{V}_{440}$	$(2\mathbf{V}_4 + \mathbf{V}_0) / 3$
$\mathbf{V}_{500}$	$(\mathbf{V}_5 + 2\mathbf{V}_0) / 3$	$\mathbf{V}_{550}$	$(2\mathbf{V}_5 + \mathbf{V}_0) / 3$
$\mathbf{V}_{600}$	$(\mathbf{V}_6 + 2\mathbf{V}_0) / 3$	$\mathbf{V}_{660}$	$(2\mathbf{V}_6 + \mathbf{V}_0) / 3$
$\mathbf{V}_{112}$	$(2\mathbf{V}_1 + \mathbf{V}_2) / 3$	$\mathbf{V}_{122}$	$(\mathbf{V}_1 + 2\mathbf{V}_2) / 3$
$\mathbf{V}_{223}$	$(2\mathbf{V}_2 + \mathbf{V}_3) / 3$	$\mathbf{V}_{233}$	$(\mathbf{V}_2 + 2\mathbf{V}_3) / 3$
$\mathbf{V}_{334}$	$(2\mathbf{V}_3 + \mathbf{V}_4) / 3$	$\mathbf{V}_{344}$	$(\mathbf{V}_3 + 2\mathbf{V}_4) / 3$
$\mathbf{V}_{445}$	$(2\mathbf{V}_4 + \mathbf{V}_5) / 3$	$\mathbf{V}_{455}$	$(\mathbf{V}_4 + 2\mathbf{V}_5) / 3$
$\mathbf{V}_{556}$	$(2\mathbf{V}_5 + \mathbf{V}_6) / 3$	$\mathbf{V}_{566}$	$(\mathbf{V}_5 + 2\mathbf{V}_6) / 3$
$\mathbf{V}_{661}$	$(2\mathbf{V}_6 + \mathbf{V}_1) / 3$	$\mathbf{V}_{611}$	$(\mathbf{V}_6 + 2\mathbf{V}_1) / 3$
$\mathbf{V}_{120}$	$(\mathbf{V}_1 + \mathbf{V}_2 + \mathbf{V}_0) / 3$	$\mathbf{V}_{450}$	$(\mathbf{V}_4 + \mathbf{V}_5 + \mathbf{V}_0) / 3$
$\mathbf{V}_{230}$	$(\mathbf{V}_2 + \mathbf{V}_3 + \mathbf{V}_0) / 3$	$\mathbf{V}_{560}$	$(\mathbf{V}_5 + \mathbf{V}_6 + \mathbf{V}_0) / 3$
$\mathbf{V}_{340}$	$(\mathbf{V}_3 + \mathbf{V}_4 + \mathbf{V}_0) / 3$	$\mathbf{V}_{610}$	$(\mathbf{V}_6 + \mathbf{V}_1 + \mathbf{V}_0) / 3$

can be seen that the abundant VVs generated by 2L-VSI and DSVM technique can effectively improve the accuracy of the output optimal VV. Thus, the system performance is improved. Furthermore, all VVs in the DSVM are defined in advance, which provides flexibility since it does not require any additional modulation schemes, such as SVPWM technique. However, for real-time applications, the computational cost of evaluating all VVs generated by DSVM is usually prohibitively high. Therefore, it is necessary to reduce the computational burden of DSVM while retaining its advantages [23], [26].

IV. PROPOSED DSVM-MPCC SCHEME

The proposed scheme integrates the flux predictive control into the pre-selection process of candidate VVs. Through tracking the stator flux increment, the pre-selection process satisfies the maximum approximation of the stator flux reference value, resulting in reduced torque ripples and current harmonics. Simultaneously, a simplified hierarchical search strategy is introduced to replace the complex look-up table in the DSVM technique, alleviating the computational burden. Furthermore, the proposed scheme employs the OSS technique to further reduce the SF losses.

A. Pre-selection of Candidate VVs

The pre-selection reference is constructed by rewriting the prediction equation of stator flux.

Firstly, according to (2), (10) can be derived

$$\frac{\mathrm{d}\psi_s}{\mathrm{d}t} = u_s - R_s i_s \tag{11}$$

It is obvious that there is a certain linear relationship between the applied stator voltage and the change rate of stator flux in the stator reference frame. Under discrete conditions, the stator flux increment can be described as

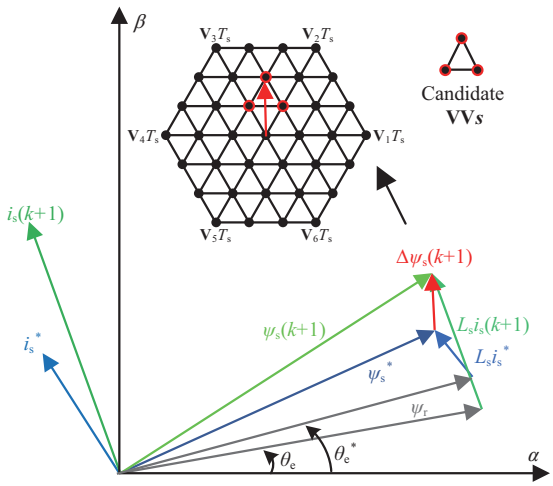

Fig. 3. Schematic diagram of pre-selection process.

$$\Delta\psi_s(k) = [u_s(k) - R_s i_s(k)]T_s \tag{12}$$

where $\Delta\psi_s(k)$ represents the stator flux increment at time k.

When the control period is small enough, the influence of stator resistance on stator flux increment can be ignored. Therefore, the stator flux increment can be considered as proportional to the stator VV. By tracking the stator flux increment, the region of the corresponding stator VVs can be obtained.

In order to maintain a fast dynamic response and reduce current harmonics as well as torque ripples, the stator flux increment is calculated according to the reference stator current. Assume that the reference current vector provided by the speed loop is i_s^*, on the basis of (3), the corresponding reference stator flux vector is

$$\psi_s^* = L_s i_s^* + \psi_r e^{j\theta_e} \tag{13}$$

where ψ_s^* represents the reference stator flux vector.

Assuming that the rotor rotates at a constant speed for a certain angle in a single cycle. Meanwhile, considering the one-step delay, the stator current $i_s(k+1)$ under the VV obtained from the optimization in previous cycle is predicted as the actual stator current at instant k. Thus, the stator flux increment in the next cycle can be defined as

$$\begin{cases} \theta_e^* = \theta_e + \omega_e T_s \\ \Delta\psi_s(k+1) = L_s[i_s^* - i_s(k+1)] + |\psi_r|(e^{j\theta_e^*} - e^{j\theta_e}) \end{cases} \tag{14}$$

Fig. 3 shows the spatial relationship between related vectors in the rotor reference frame. On the basis of (14), the stator flux increment which meet the need of control demand in the next cycle can be calculated approximately. At the same time, all VVs generated by the DSVM technique can be considered as evenly distributed in space. The whole vector space can be regarded as composed of equilateral triangles, each containing three

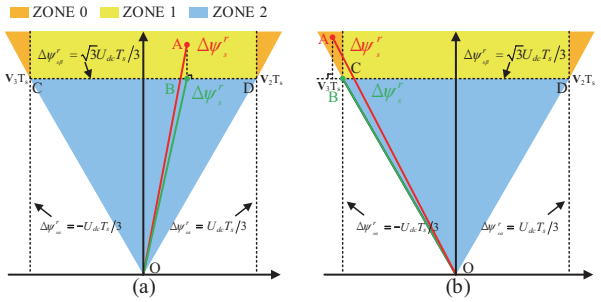

Fig. 4. Schematic diagram of over-modulation strategy.

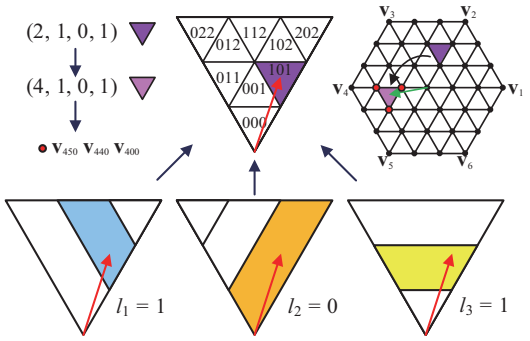

Fig. 5. Schematic diagram of hierarchical search strategy.

available VVs. According to the calculated stator flux increment, an explicit equilateral triangle region can be obtained. The three VVs corresponding to this region are taken as candidate VVs. The optimal VV will be generated by evaluation. According to (11), the output optimal VV can meet the stator flux increment to the greatest extent. Therefore, the whole system can have less torque ripples and current harmonics.

To ensure the precise tracking of the reference VV, a suitable VV overflow constraint will be implemented to guarantee that the optimal VV remains within the modulation region. Firstly, to reduce the complexity of the vector operations, the reference stator flux increment is reconstructed in Sector II as

$$\Delta\psi_s^r = \Delta\psi_s e^{j[(2-s)\pi/3]} \tag{15}$$

where $\Delta\psi_s^r$ is the reconstructed stator flux increment.

As shown in Fig. 4, ZONE 0 and ZONE 1 are the zones beyond the modulation region. Suppose the reconstructed stator flux increment is vector OA in Fig. 4(a), which is located in ZONE 1. In this case, the stator flux increment will be pulled back to the point B, which is the intersection of point A and the vertical line of line CD. Then the vector OB can be seen as the desired stator flux increment in the linear modulation area. Similarly, in ZONE 0, since the intersection of the vertical lines falls outside the linear modulation area, the nearest point to the intersection of the vertical lines on the CD line is used to form the desired stator flux increment. The specific constraint strategy is

$$\begin{cases} \Delta\psi_{s\alpha}^r = \begin{cases} \Delta\psi_{s\alpha}^r, & |\Delta\psi_{s\alpha}^r| \leqslant \dfrac{U_{dc}T_s}{3} \\ \text{sign}(\Delta\psi_{s\alpha}^r)\dfrac{U_{dc}T_s}{3}, & |\Delta\psi_{s\alpha}^r| > \dfrac{U_{dc}T_s}{3} \end{cases} \\ \Delta\psi_{s\beta}^r = \begin{cases} \Delta\psi_{s\beta}^r, & \Delta\psi_{s\beta}^r \leqslant \dfrac{\sqrt{3}U_{dc}T_s}{3} \\ \dfrac{\sqrt{3}U_{dc}T_s}{3}, & \Delta\psi_{s\beta}^r > \dfrac{\sqrt{3}U_{dc}T_s}{3} \end{cases} \end{cases} \tag{16}$$

where sign(x) represents symbolic function.

B. Simplified DSVM Technique

In classical DSVM applications [22], [23], all generated VVs are usually stored in a look-up table in advance, however, it can be known from (10) that the capacity of the look-up table will rise rapidly and become complex as N rises. In addition, some studies locate candidate VVs by constructing auxiliary lines or solving evaluation functions, but the process of generating the switching states of these VVs is very tedious. In order to solve these problems, a hierarchical search strategy is used to simplify the DSVM technique.

TABLE II
SECTOR AND CORRESPONDING VVS

Sector Number	1	2	3	4	5	6
(V_x, V_y)	(V_1, V_2)	(V_2, V_3)	(V_3, V_4)	(V_4, V_5)	(V_5, V_6)	(V_6, V_1)

The main objective of the hierarchical search strategy is to determine an equilateral triangle region based on the reconstructed stator flux increment and to obtain three candidate VVs at the vertices of this equilateral triangle. Therefore, each equilateral triangle region can be recorded by a set of indexes (s, l_1, l_2, l_3), where s is the sector of the actual stator flux increment, l_1, l_2, l_3 are the different levels of the reconstructed stator flux increment in Sector II. They can be expressed as

$$\begin{cases} l_1 = \text{round}\left[\dfrac{(3\Delta\psi_{s\alpha}^r + \sqrt{3}\Delta\psi_{s\beta}^r)N}{2U_{dc}T_s}\right] \\ l_2 = \text{round}\left[\dfrac{(3\Delta\psi_{s\alpha}^r - \sqrt{3}\Delta\psi_{s\beta}^r)N}{2U_{dc}T_s}\right] \\ l_3 = \text{round}\left[\dfrac{\sqrt{3}\Delta\psi_{s\beta}^r N}{U_{dc}T_s}\right] \end{cases} \tag{17}$$

where round(x) represents rounding operation.

Since the whole vector space is a uniform positive hexagon, the hierarchical distribution obtained in sector 2 will be consistent with the other sector cases. As shown in Fig. 5, a unique set of indexes can be determined by the sector number and (17). Meanwhile, the hierarchical distribution of each equilateral triangle also reflects the spatial position of the candidate VVs, so that the three candidate VVs can be calculated by the hierarchical number as

$$\begin{cases} \tau = (l_1 + l_2 + l_3)\%2 \\ \mathrm{V}(1) = [(l_1 + \tau)\mathrm{V}_x + (l_2 + \tau)\mathrm{V}_y]/N \\ \mathrm{V}(2) = [l_1\mathrm{V}_x + (l_2 + 1)\mathrm{V}_y]/N \\ \mathrm{V}(3) = [(l_1 + 1)\mathrm{V}_x + l_2\mathrm{V}_y]/N \end{cases} \tag{18}$$

where % represents modular arithmetic; V_x, V_y represent the boundary VV of the sector of the actual stator flux increment. Table II shows V_x, V_y and the corresponding sector number.

Afterwards, on the basis of the stator current at instant k+1 which consider the digital delay compensation, the optimal VV can be evaluated from the three candidate VVs according to (6) to reduce the torque and flux ripples. Moreover, the proposed strategy can maintain constant computational complexity as N varies, which enhances the flexibility of DSVM technique.

C. Pulse Generation With Reduced Switching Frequency

A switching frequency (SF) reduction strategy is also employed in the proposed scheme to reduce the switching losses [23]. The strategy consists of two aspects of optimization: 1) the SF reduction during the current control cycle; 2) the SF reduction during different control cycles. Firstly, according to the above discussion, the output optimal VV evaluated from (18) can be described as

$$\mathrm{V}_{\mathrm{opt}} = \frac{\lambda_0 \mathrm{V}_{0/7} + \lambda_1 \mathrm{V}_x + \lambda_2 \mathrm{V}_y}{N}, N = \lambda_0 + \lambda_1 + \lambda_2 \tag{19}$$

where $\lambda_{i,i=0,1,2}$ is the number of control intervals in which the basic VV operates according to (18).

It can be seen that the optimal VV may be composed of one, two, or three basic VVs in a single control cycle. Thus, to clarify the composition of the optimal VV, we can define

$$\lambda = \eta(\lambda_0) + 2\eta(\lambda_1) + 4\eta(\lambda_2), \eta(x) = \begin{cases} 0, x = 0 \\ 1, x \neq 0 \end{cases} \tag{20}$$

According to the principle that only one phase of the inverter changes in each switching, the candidate optimal switching sequences (OSS) for each λ can be obtained in advance, which are listed in Table III. Furthermore, if the candidate OSS are not unique, the optimal OSS is selected as the one that satisfies the minimization of switching losses in the adjacent control cycle, which can be described as

$$\mathrm{OSS}_{\mathrm{opt}} = \arg\min\left\{ \sum_{x=\{a,b,c\}} \left| S_{x,i} - S_{x,\mathrm{last}} \right| \right\} \tag{21}$$

where $S_{x,i}$ is the first switching state of the candidate OSS which i represents the index of the candidate OSS; $S_{x,\mathrm{last}}$ is the last switching state of the previous OSS.

As depicted in Fig. 6, assuming that the last OSS is V_7-V_4-V_5, and the value of λ is 3, sector is 5, then the current OSS will be selected as V_5-V_0 based on (21) and Table III. The proposed OSS strategy can minimize the SF losses during the whole control process, while the system performance is not affected due to only the reconstruction of VVs.

TABLE III
SELECTION OF CANDIDATE OSS

λ	Candidate optimal switching sequences	
	Sector=1,3,5	Sector=2,4,6
1	V_0 or V_7	V_0 or V_7
2	V_x	V_x
3	V_0-V_x or V_x-V_0	V_7-V_x or V_x-V_7
4	V_y	V_y
5	V_7-V_y or V_y-V_7	V_0-V_y or V_y-V_0
6	V_x-V_y or V_y-V_x	V_x-V_y or V_y-V_x
7	V_x-V_y-V_7 or V_y-V_x-V_0 V_0-V_x-V_y or V_7-V_y-V_x	V_x-V_y-V_0 or V_y-V_x-V_7 V_7-V_x-V_y or V_0-V_y-V_x

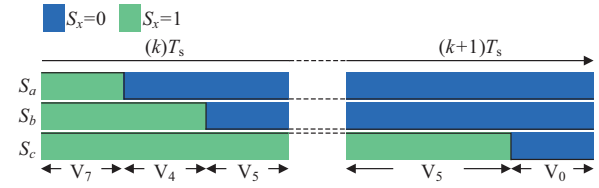

Fig. 6. Schematic diagram of OSS strategy.

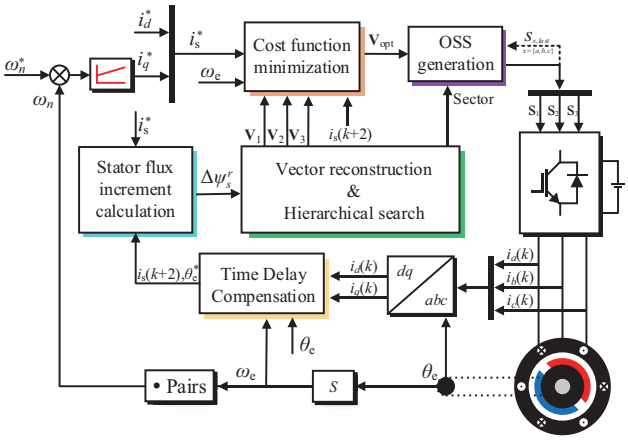

Fig. 7. System structure of the proposed scheme.

D. Discussion

The proposed scheme demonstrates a reliable and low-complexity pre-selection method for DSVM-MPCC. Moreover, it mitigates the switching losses by employing the OSS strategy. The control block diagram of the proposed scheme is illustrated in Fig. 7, which can be summarized as follows: 1) Measurements of the phase current, motor speed and, electrical angle; 2) Time delay compensation for predicted currents and angle; 3) Calculation of the stator flux increment; 4) Reconstruction of the stator flux increment vector and identification of the candidate VVs using the hierarchical search strategy; 5) Evaluation of the optimal VV; 6) Selection and output of the OSS.

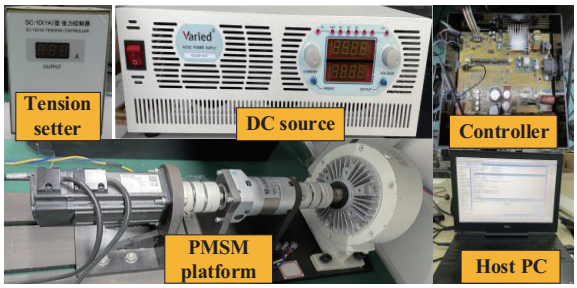

Fig. 8. Experimental platform.

TABLE IV
PARAMETER OF THE EXPERIMENTAL SYSTEM

Parameters	Symbol	Numeric Value
DC voltage	u_{dc}	320 V
d-axis inductance	L_d	6.5 mH
q-axis inductance	L_q	6.5 mH
Stator Resistance	R_s	2.35 Ω
Rotor flux	ψ_f	0.07876 Wb
Pole pairs	p	4
Inertia coefficient	J	0.0003 kg·m^2
Rated speed	ω_{nom}	3000 r/min
Rated torque	T_{nom}	1.27 N·m
Sample time	T_s	0.0001 s
PI gain of Speed loop	k_p, k_i	k_p= 0.6, k_i= 0.05

V. EXPERIMENTAL RESULTS

The validity of the proposed DSVM-MPCC is proven experimentally on a surface-mounted PMSM drive platform shown in Fig. 8. The platform uses a Texas Instruments 32-bit DSP TMS320F28335 as the main control unit. Relevant parameters of the control system are listed in Table IV. The proposed scheme is compared with the conventional MPCC (C-MPCC), 38VVs-DSVM-based MPCC (DSVM-0), DSVM-1 [23], DSVM-2 [24], DSVM-DB [26] in terms of performance, complexity, and flexibility. For a fair comparison, the PI parameter of the speed loop is the same and the control mode of i_d^*=0 is used for all schemes.

A. Calculational Burden Analysis

The execution time of each state of the algorithm is tested separately to evaluate the computational burden. To ensure the consistency of the measurements, all algorithms are written in C language and the compiler optimization level is set to 0. The measurement results are shown in Fig. 9. It can be seen that the execution time of the proposed scheme and DSVM-DB [26] is significantly smaller than DSVM-0, DSVM-1 [23], and DSVM-2 [24] due to the pre-selection strategy. And the computational effort of the proposed scheme is further reduced compared to DSVM-DB [26], which is close to C-MPCC. The execution time of the proposed scheme is 11.18 μs, whereas the execution time of DSVM-0, DSVM-1 [23], DSVM-2 [24], DSVM-DB [26] is 41.03, 25.70, 23.82 and16.53 μs, respectively.

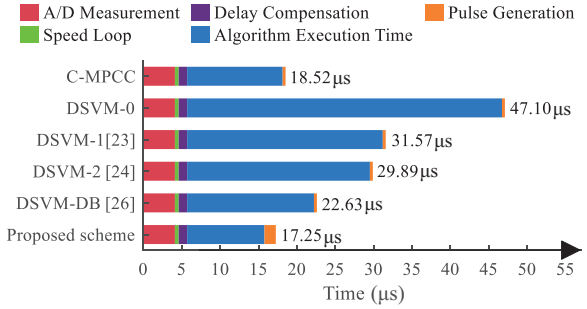

Fig. 9. Algorithm execution time analysis.

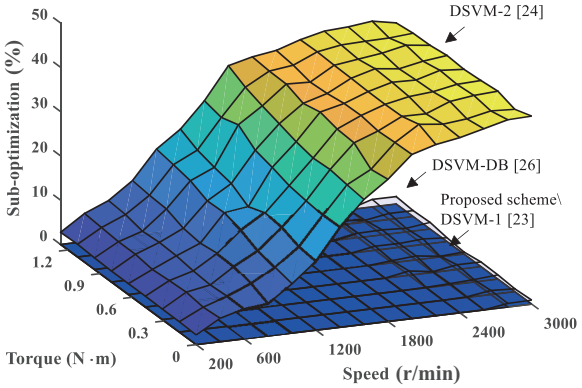

Fig. 10. Sub-optimization analysis.

B. Sub-optimization Analysis

The suboptimality reflects the performance loss of the simplified DSVM-MPC compared to the conventional DSVM strategy [23]. Hence, suboptimality can be defined as

$$\text{Suboptimality} = \begin{cases} 0, & |g_M = g_{DSVM-0}| \\ \sum_1^{\infty} n, & \text{otherwise} \end{cases} \tag{22}$$

where g_M is the value of cost function of the tested scheme and g_{DSVM-0} represents that of the conventional scheme.

The sub-optimization is defined as the ratio of suboptimality, as shown in Fig. 10. It can be seen that DSVM-2 [24] has a higher sub-optimization due to inaccurate sector prediction. Also, DSVM-DB [26] cannot maintain constant accurate prediction within whole operating range due to the lack of proper VV overflow handle. The sub-optimization of proposed scheme and DSVM-1 [23] remains 0 over the entire range, which means the proposed scheme fully inherit the advantages of DSVM technique.

C. Evaluation of Different N Values and Switching Frequency

Fig. 11 shows the THD and average switching frequency (ASF) of the proposed scheme with and without OSS under different N values at 1000 r/min. It is observed that as N increases, the THD is significantly reduced while the ASF increases. This illustrates that the proposed scheme can

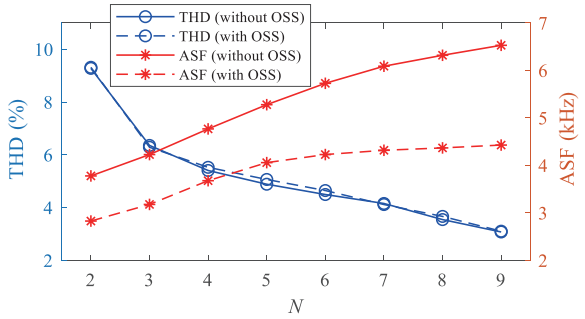

Fig. 11. THD and average switching frequency (ASF) of the proposed scheme at different *N*.

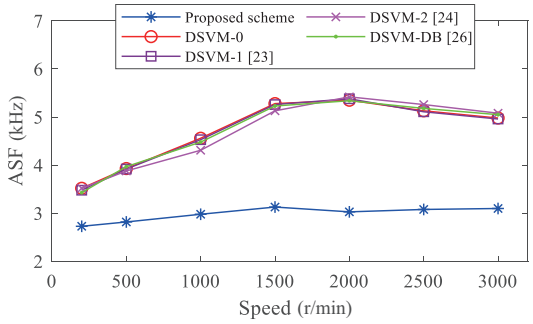

Fig. 12. Average switching frequency (ASF) of the different scheme under different speed.

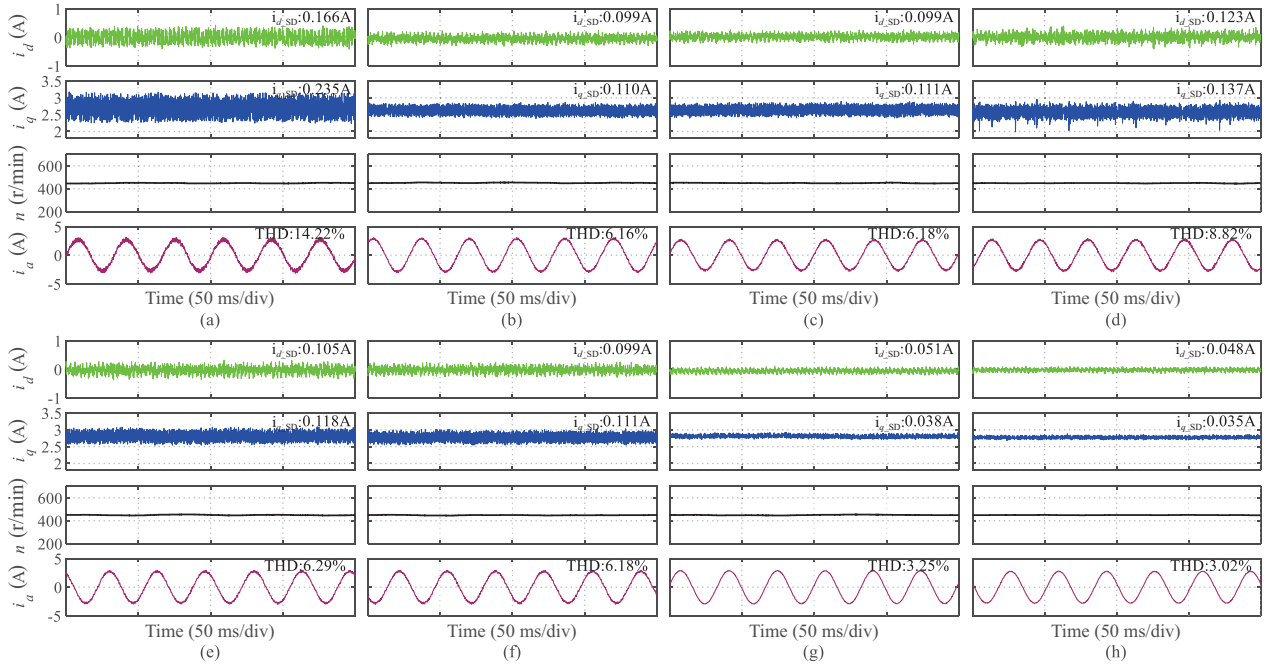

Fig. 13. Comparison of steady-state performance at 450 r/min. (a) C-MPCC. (b) DSVM-0. (c) DSVM-1 [23]. (d) DSVM-2 [24]. (e) DSVM-DB [26]. (f) the proposed scheme. (g) DSVM-DB [26] (*N*=9). (h) the proposed scheme (*N*=9).

decouple the control period from the switching frequency without increased computational burden. Furthermore, it is also evident that the use of OSS strategy notably decreases the ASF without causing any degradation in control performance for the proposed scheme. Fig. 12 further provides the comparative results of the ASF for several schemes under different speeds, with the *N* value is set to 3. At the same control period, the ASF of the proposed scheme with OSS ranges from 2.7 to 3.2 kHz, which is significantly lower than other DSVM schemes. It is obvious that the proposed scheme effectively reduces the switching losses and enhances the flexibility of DSVM technique.

D. Steady-state Performance Comparison

Fig. 13 and Fig. 14 show the steady-state performance of several control schemes at 450 r/min and 3000 r/min with rated load. The waveforms of *d-q* axis stator current, speed and Phase-A current are included in the figure. In addition, the FFT-analysis is performed and the standard deviation (SD) of *d-q* axis stator current is calculated for further evaluation as

$$i_{d,q\_\mathrm{SD}} = \sqrt{\frac{1}{n}\sum_{i=0}^{n}[i_{d,q}(i) - i_{d,q}^{\mathrm{ave}}]^2}, i_{d,q}^{\mathrm{ave}} = \frac{1}{n}\sum_{i=0}^{n} i_{d,q}(i) \qquad (23)$$

From Fig. 13(a)-(f), it can be seen that the DSVM-MPC methods achieve lower current ripples and total harmonic distortion (THD) compared to C-MPCC. At 450 r/min, the *d-q* axis stator current ripples of the proposed scheme are 0.099 A and 0.111 A, and the THD is 6.18%, which is similar to DSVM-0, DSVM-1 [23] and better than DSVM-2 [24]. At 3000 r/min, both the *d-q* axis stator current ripples and THD are smaller in the proposed scheme compared to DSVM-DB [26], which indicates that the proposed scheme is not affected by the increased modulation index under the high-speed, heavy-load conditions. In addition, the proposed scheme presents better steady-state performance at *N*=9 with the same

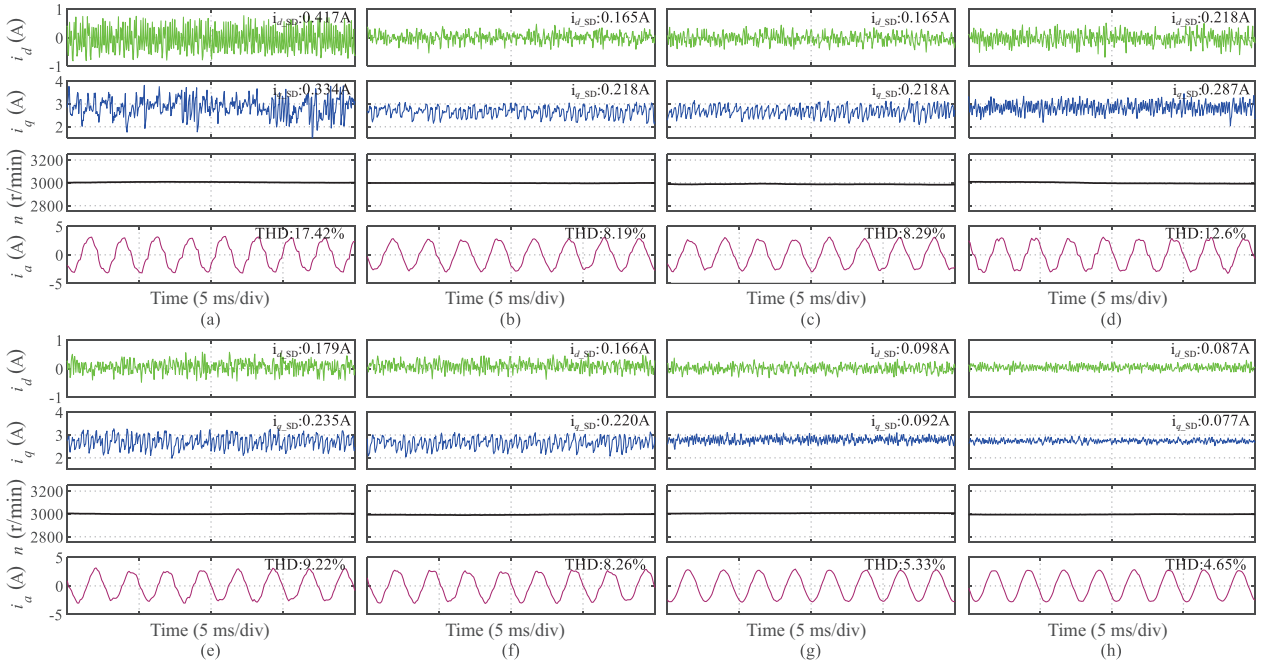

Fig. 14. Comparison of steady-state performance at 3000 r/min. (a) C-MPCC. (b) DSVM-0. (c) DSVM-1 [23]. (d) DSVM-2 [24]. (e) DSVM-DB [26]. (f) the proposed scheme. (g) DSVM-DB [26] (N=9). (h) the proposed scheme (N=9).

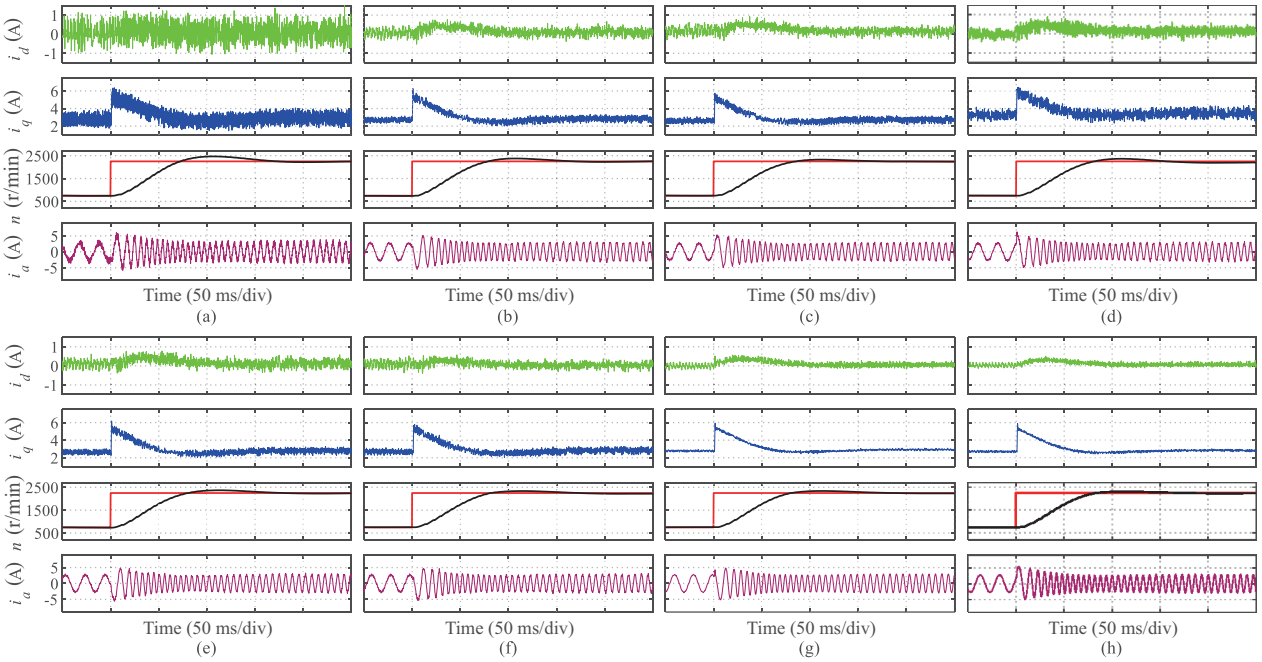

Fig. 15. Comparison of dynamic-state performance at sudden speed change. (a) C-MPCC. (b) DSVM-0. (c) DSVM-1 [23]. (d) DSVM-2 [24]. (e) DSVM-DB [26]. (f) the proposed scheme. (g) DSVM-DB [26] (N=9). (h) the proposed scheme (N=9).

computational burden as before, which can be seen in Fig. 14(g), (h). Meanwhile, the application of the OSS strategy allows the proposed scheme to maintain a lower ASF while obtaining the excellent steady-state performance.

E. Dynamic Performance Comparison

The dynamic performance is verified by imposing sudden changes in q-axis stator current and speed, respectively. Fig. 15 presents the waveforms when the reference speed is stepped from 750 r/min to 2250 r/min. It can be seen that the dynamic performance of the proposed scheme is similar to DSVM-0. And compared with C-MPCC and DSVM-2 [24], the proposed scheme is able to maintain lower d-q axis stator current ripples and smoother Phase-A current during the sudden speed change.

Fig. 16 shows the dynamic waveforms when the given q-axis

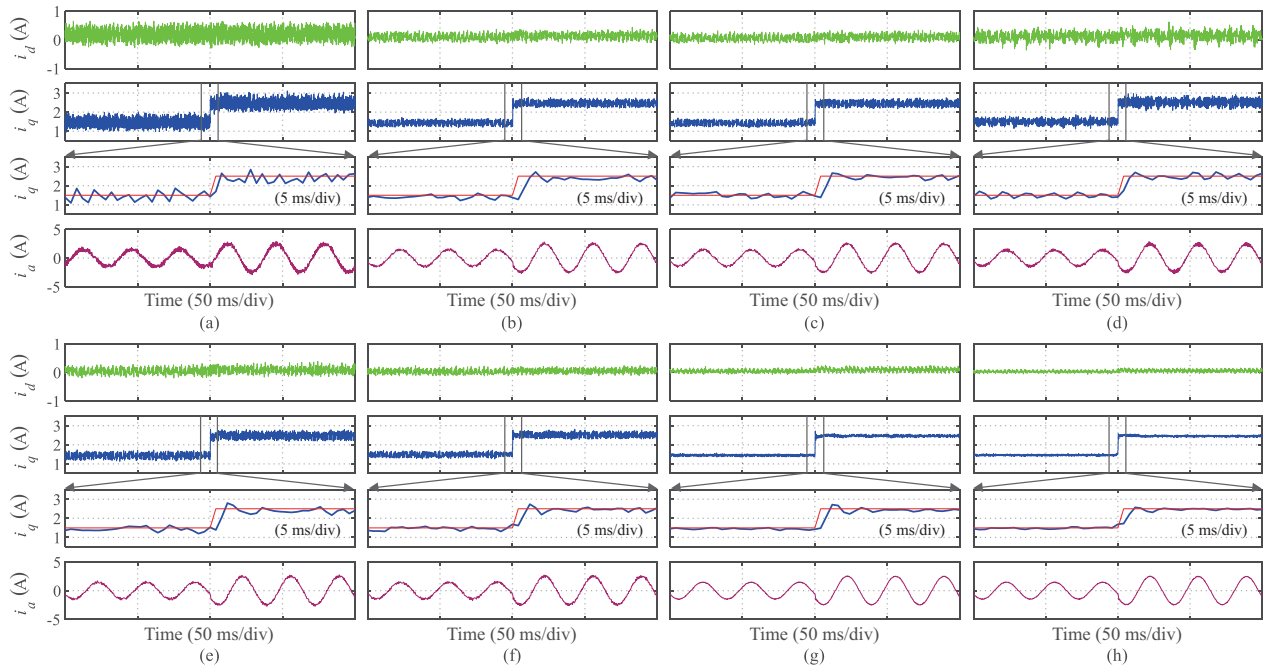

Fig. 16. Comparison of dynamic-state performance at sudden *q*-axis stator current change. (a) C-MPCC. (b) DSVM-0. (c) DSVM-1 [23]. (d) DSVM-2 [24]. (e) DSVM-DB [26]. (f) the proposed scheme. (g) DSVM-DB [26] (N=9). (h) the proposed scheme (N=9).

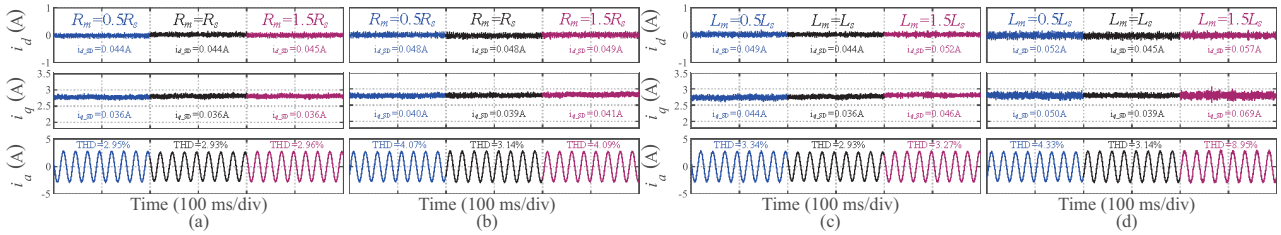

Fig. 17. Comparative experimental results of parameter mismatch. (a)(c): the proposed scheme. (b)(d): DSVM-DB [26].

stator current surges from 1.5 A to 2.5 A. From Fig. 16(a)-(f), it can be seen that the proposed scheme is significantly more effective than C-MPCC and DSVM-2 [24] in attenuating the *d*-*q* axis stator current ripples. Furthermore, it can be seen from Fig. 16(g), (h) that the proposed scheme further reduces the *q*-axis stator current ripples compared to DSVM-DB [26].

F. Evaluation of Parameter Robustness

Fig. 17 presents the results of robustness evaluation for the proposed scheme and DSVM-DB [26] under the situations of stator resistance and inductance mismatch. The speed is 600 r/min and N is set to 9. Fig.17(a), (b) shows the control performance under resistance mismatch, and it can be seen that the proposed scheme is almost unaffected by the change of stator resistance parameter. Fig. 17(c), (d) shows the results when the inductance is detuned to be $0.5L_s$ and $1.5L_s$, respectively. Compared with the DSVM-DB [26], the control performance of the proposed scheme is less affected by the inductance mismatch, which can be observed from its low stator current ripples and low current harmonics. Therefore, the proposed scheme has low parameter sensitivity and is robust for parameter variations.

Overall, as shown in Table V, the merits of the proposed method include

(1) Compared with the conventional FCS-MPCC, the proposed method yields lower torque and flux ripples as well as THD of phase current by obtaining more precise optimal VV.

(2) The proposed method carries a decreased computational burden relative to existing DSVM-MPCC methods, which remains constant even as the number of virtual VVs increases.

(3) With the adoption of the OSS strategy, the proposed method effectively reduces the switching frequency.

VI. Conclusion

An enhanced DSVM-based FCS-MPCC control method is proposed in this paper and has been validated experimentally on a PMSM platform. In comparison to existing DSVM-MPC methods, the proposed approach reduces the computational burden effectively while minimizing torque and flux ripples through the use of a novel VV pre-selection scheme. Furthermore, the switching losses are further mitigated without compromising the control performance, thanks to the SF

TABLE V
COMPARISON OF DIFFERENT METHODS

Methods	Enumeration Numbers	Computational Complexity	Torque and Flux Ripples	THD of Phase Current	Average Switching Frequency
C-MPCC	8	Low	High	High	Low
DSVM-0	38	High (Increase with rising N)	Low	Low	High
DSVM-1 [23]	13	Medium (Increase with rising N)	Low	Low	High
DSVM-2 [24]	12	Medium (Increase with rising N)	Medium	Medium	High
DSVM-DB [26]	3	Medium (Constant with rising N)	Between low and medium	Between low and medium	High
Proposed Method	3	Low (Constant with rising N)	Low	Low	Low

reduction strategy. Consequently, the proposed method brings great improvement for FCS-MPC schemes.

REFERENCES

[1] X. Sun, M. Wu, G. Lei, Y. Guo, and J. Zhu, "An improved model predictive current control for PMSM drives based on current crack circle," in *IEEE Transactions on Industrial Electronics*, vol. 68, no. 5, pp. 3782–3793, May 2021.

[2] R. Zhang, Z. Yin, J. Liu, and S. Yu, "Low carrier wave ratio modulation strategy of permanent magnet synchronous motor based on metro traction system: A comparative study," in *CPSS Transactions on Power Electronics and Applications*, vol. 7, no. 1, pp. 1–16, Mar. 2022.

[3] Y. Xu, Z. Yan, Y. Zhang, and R. Song, "Model predictive current control of permanent magnet synchronous motor based on sliding mode observer with enhanced current and speed tracking ability under disturbance," in *IEEE Transactions on Energy Conversion*, vol. 38, no. 2, pp. 948–958, Jun. 2023.

[4] Z. Chen, T. Shi, Z. Lin, Z. Wang, and X. Gu, "Analysis and control of current harmonic in IPMSM field-oriented control system," in *IEEE Transactions on Power Electronics*, vol. 37, no. 8, pp. 9571–9585, Aug. 2022.

[5] Q. Teng, H. Yang, and J. Tian, "Nonlinear function integral sliding mode-based model predictive current control for PMSM drives with DC-bus voltage observer," in *CPSS Transactions on Power Electronics and Applications*, vol. 7, no. 4, pp. 399–408, Dec. 2022.

[6] A. A. Ahmed, B. K. Koh, and Y. I. Lee, "A comparison of finite control set and continuous control set model predictive control schemes for speed control of induction motors," in *IEEE Transactions on Industrial Informatics*, vol. 14, no. 4, pp. 1334–1346, Apr. 2018.

[7] J. Rodriguez, C. Garcia, A. Mora, F. Flores-Bahamonde, P. Acuna, M. Novak, Y. Zhang, L. Tarisciotti, S. A. Davari, Z. Zhang, *et al*., "Latest advances of model predictive control in electrical drives—Part I: basic concepts and advanced strategies," in *IEEE Transactions on Power Electronics*, vol. 37, no. 4, pp. 3927–3942, Apr. 2022.

[8] P. Karamanakos and T. Geyer, "Guidelines for the design of finite control set model predictive controllers," in *IEEE Transactions on Power Electronics*, vol. 35, no. 7, pp. 7434–7450, Jul. 2020.

[9] W. Deng, J. Tang, and W. Cheng, "An enhanced rotating vector-based direct torque control for matrix converter-fed PMSM drives using virtual pulsating vectors," in *CPSS Transactions on Power Electronics and Applications*, vol. 8, no. 1, pp. 65–73, Mar. 2023.

[10] X. Zhang, L. Zhang, and Y. Zhang, "model predictive current control for PMSM drives with parameter robustness improvement," in *IEEE Transactions on Power Electronics*, vol. 34, no. 2, pp. 1645–1657, Feb. 2019.

[11] J. Gao, C. Gong, W. Li, and J. Liu, "novel compensation strategy for calculation delay of finite control set model predictive current control in PMSM," in *IEEE Transactions on Industrial Electronics*, vol. 67, no. 7, pp. 5816–5819, Jul. 2020.

[12] X. Zhang, X. Wu, G. Tan, W. Zhang, and Q. Wang, "A dual-vector model predictive control method with minimum current THD," in *IEEE Transactions on Power Electronics*, vol. 36, no. 9, pp. 9758–9762, Sept. 2021.

[13] M. Wu, X. Sun, J. Zhu, G. Lei, and Y. Guo, "Improved model predictive torque control for PMSM drives based on duty cycle optimization," in *IEEE Transactions on Magnetics*, vol. 57, no. 2, pp. 1–5, Feb. 2021.

[14] J. Chen, Y. Qin, A. M. Bozorgi, and M. Farasat, "Low complexity dual-vector model predictive current control for surface-mounted permanent magnet synchronous motor drives," in *IEEE Journal of Emerging and Selected Topics in Power Electronics*, vol. 8, no. 3, pp. 2655–2663, Sept. 2020.

[15] Y. Zhang, D. Xu, and L. Huang, "Generalized multiple-vector-based model predictive control for PMSM drives," in *IEEE Transactions on Industrial Electronics*, vol. 65, no. 12, pp. 9356–9366, Dec. 2018.

[16] X. Li, Z. Xue, L. Zhang, and W. Hua, "A low-complexity three-vector-based model predictive torque control for SPMSM," in *IEEE Transactions on Power Electronics*, vol. 36, no. 11, pp. 13002–13012, Nov. 2021.

[17] S. G. Petkar and V. K. Thippiripati, "Effective multi-vector operated predictive current control of PMSM drive with reduced torque and flux ripple," in *IEEE Transactions on Transportation Electrification*, vol. 9, no. 2, pp. 2217–2227, Jun. 2023.

[18] S. -W. Kang, J. -H. Soh, and R. -Y. Kim, "Symmetrical three-vector-based model predictive control with deadbeat solution for IPMSM in rotating reference frame," in *IEEE Transactions on Industrial Electronics*, vol. 67, no. 1, pp. 159–168, Jan. 2020.

[19] B. Xu, Q. Jiang, W. Ji, and S. Ding, "An improved three-vector-based model predictive current control method for surface-mounted PMSM drives," in *IEEE Transactions on Transportation Electrification*, vol. 8, no. 4, pp. 4418–4430, Dec. 2022.

[20] T. Li, R. Ma, and W. Han, "Virtual-vector-based model predictive current control of five-phase PMSM with stator current and concentrated disturbance observer," in *IEEE Access*, vol. 8, pp. 212635–212646, 2020.

[21] I. Gonzalez-Prieto, M. J. Duran, J. J. Aciego, C. Martin, and F. Barrero, "Model predictive control of six-phase induction motor drives using virtual voltage vectors," in *IEEE Transactions on Industrial Electronics*, vol. 65, no. 1, pp. 27–37, Jan. 2018.

[22] I. Osman, D. Xiao, M. F. Rahman, M. Norambuena, and J. Rodriguez, "Discrete space vector modulation based model predictive flux control with reduced switching frequency for IM drive," in *IEEE Transactions on Energy Conversion*, vol. 36, no. 2, pp. 1357–1367, Jun. 2021.

[23] I. Osman, D. Xiao, K. S. Alam, S. M. S. I. Shakib, M. P. Akter and M. F. Rahman, "Discrete space vector modulation-based model predictive torque control with no suboptimization," in *IEEE Transactions on Industrial Electronics*, vol. 67, no. 10, pp. 8164–8174, Oct. 2020.

[24] M. Amiri, J. Milimonfared, and D. A. Khaburi, "Predictive torque control implementation for induction motors based on discrete space vector modulation," in *IEEE Transactions on Industrial Electronics*, vol. 65, no. 9, pp. 6881–6889, Sept. 2018.

[25] W. Zhang, Y. Yang, M. Fan, L. He, A. Ji, Y. Xiao, H. Wen, X. Zhang, T. Yang, S. Mekhilef, *et al*., "An improved model predictive torque control

for PMSM drives based on discrete space vector modulation," in *IEEE Transactions on Power Electronics*, vol. 38, no. 6, pp. 7535–7545, Jun. 2023.

[26] Y. Wang, X. Wang, W. Xie, F. Wang, M. Dou, R. M. Kennel, R. D. Lorenz, and D. Gerling, "Deadbeat model-predictive torque control with discrete space-vector modulation for PMSM drives," in *IEEE Transactions on Industrial Electronics*, vol. 64, no. 5, pp. 3537–3547, May 2017.

[27] W. Wang, C. Liu, S. Liu, and H. Zhao, "Model predictive torque control for dual three-phase PMSMs with simplified deadbeat solution and discrete space-vector modulation," in *IEEE Transactions on Energy Conversion*, vol. 36, no. 2, pp. 1491–1499, Jun. 2021.

[28] H. -C. Moon, J. -S. Lee, and K. -B. Lee, "A robust deadbeat finite set model predictive current control based on discrete space vector modulation for a grid-connected voltage source inverter," in *IEEE Transactions on Energy Conversion*, vol. 33, no. 4, pp. 1719–1728, Dec. 2018.

[29] Y. Zhang, H. Jiang, and H. Yang, "Model predictive control of PMSM drives based on general discrete space vector modulation," in *IEEE Transactions on Energy Conversion*, vol. 36, no. 2, pp. 1300–1307, Jun. 2021.

[30] T. Jin, H. Song, P. G. Ipoum-Ngome, D. L. Mon-Nzongo, J. Tang, M. Zhu, and J. Rodriguez, "Low complexity model predictive flux control based on discrete space vector modulation and optimal switching sequence for induction motors," in *IEEE Transactions on Industrial Electronics*, vol. 71, no. 1, pp. 305–315, Jan. 2024.

[31] I. M. Alsofyani and K. -B. Lee, "A unidirectional voltage vector preselection strategy for optimizing model predictive torque control with discrete space vector modulation of IPMSM," in *IEEE Transactions on Industrial Electronics*, vol. 69, no. 12, pp. 12305–12315, Dec. 2022.

Jun Sun received the B.S. degree in engineering from Soochow University, Suzhou, China, in 2021. He is currently pursuing the M.S. degree in engineering at School of Rail Transportation, Soochow University, Suzhou, China.

His research interest includes model predictive control for motor drives.

Yong Yang received the B.S. degree in automation from Xiangtan University, Xiangtan, China, in 2003, the M.S. degree in Electrical Engineering from Guizhou University, Guiyang, China, in 2006, and the Ph.D. degree in Electrical Engineering from Shanghai University, Shanghai, China, in 2010.

He is currently a full Professor with the School of Rail Transportation, Soochow University. From December 2017 to December 2018, he was a Visiting Scholar with Center for High Performance Power Electronics (CHPPE) of The Ohio State University, Columbus, USA. He has coauthored more than 100 journal and conference papers. His current research interests include model predictive control in power electronic converters, distributed energy resource interfacing and high-performance motor drive control.

Jiefeng Hu received the Ph.D. degree in electrical engineering from University of Technology Sydney (UTS), Australia, in 2013. He participated in the research of minigrids in Commonwealth Scientific and Industrial Research Organization, Newcastle, Australia. He was an Assistant Professor with The Hong Kong Polytechnic University, Kowloon, Hong Kong. He is currently an Associate Professor and a Program Coordinator of Electrical Engineering with Federation University Australia, Ballarat, VIC, Australia, where he is also the Stream Leader of Centre for New Energy Transition Research. His research interests include power electronics, renewable energy, and smart microgrids. Dr. Hu is an Associate Editor for *IET Renewable Power Generation*, an Editor for *IEEE Transactions on Energy Conversion*, an Associate Editor for *IEEE Access*, and was a Guest Editor for *IEEE Transactions on Industrial Electronics* for a Special Issue "Applications of Predictive Control in Microgrids."

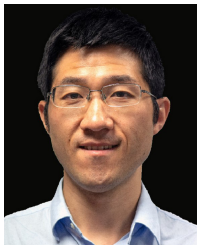

Xinan Zhang received the B.E. degree in electrical engineering and automation from Fudan University, China, in 2008. He received the Ph.D. degree from Nanyang Technological University (NTU), Singapore, in 2014. Then, he worked as postdoc researcher in NTU and the University of New South Wales from 2014 to 2017. He worked as a Lecturer in NTU from June 2017 to September 2019.

Since September 2019, he joined the University of Western Australia as a Senior Lecturer. His research interests include electrical machine drives, control and modulation of power electronic converters and design of hybrid energy storage systems.

Xinghe Li received the B.S. degree in automation from Xiangtan University, Xiangtan, China, in 2003, the M.S. degree in Biomedical Engineering from Shandong University, Jinan, China, in 2006.

He is currently working as a Product Management Department director and a professor level engineer at Shanghai Sigriner STEP Electric Co., Ltd. He has received 42 authorized invention patents and published 12 papers. His current research interests include high performance motor drive control and embedded software system.

Jose Rodriguez received the Engineer degree in electrical engineering from the Universidad Tecnica Federico Santa Maria, in Valparaiso, Chile, in 1977 and the Dr.-Ing. degree in electrical engineering from the University of Erlangen, Erlangen, Germany, in 1985. He has been with the Department of Electronics Engineering, Universidad Tecnica Federico Santa Maria, since 1977, where he was full Professor and President. Since 2015 to 2019 he was the President of Universidad Andres Bello in Santiago, Chile. Since 2022 to 2023 he was President of Universidad San Sebastian in Santiago, Chile. Now, he is the Director of the Center for Energy Transition at Universidad San Sebastian. He has coauthored two books, several book chapters and more than 900 journal and conference papers. His main research interests include multilevel inverters, new converter topologies, control of power converters, and adjustable-speed drives. He has received a number of best paper awards from journals of the IEEE. Dr. Rodriguez is member of the Chilean Academy of Engineering. In 2014 he received the National Award of Applied Sciences and Technology from the government of Chile. In 2015 he received the Eugene Mittelmann Award from the Industrial Electronics Society of the IEEE. In years 2014 to 2023 he has been included in the list of Highly Cited Researchers published by Web of Science.